Towards topological quasifreestanding stanene via substrate engineering

Domenico Di Sante,[1,*] Philipp Eck,[1] Maximilian Bauernfeind,[2] Marius Will,[2] Ronny Thomale,[1] Jörg Schäfer,[2] Ralph Claessen,[2] and Giorgio Sangiovanni[1]

[1]*Institut für Theoretische Physik und Astrophysik, Universität Würzburg, Am Hubland Campus Süd, Würzburg 97074, Germany*

[2]*Physikalisches Institut and Röntgen Research Center for Complex Material Systems, Universität Würzburg, Am Hubland Campus Süd, Würzburg 97074, Germany*

(Received 26 July 2018; published 23 January 2019)

In search for a new generation of spintronics hardware, material candidates for room temperature quantum spin Hall effect (QSHE) have become a contemporary focus of investigation. Inspired by the original proposal for QSHE in graphene, several heterostructures have been synthesized, aiming at a hexagonal monolayer of heavier group IV elements promoting the QSHE bulk gap via increased spin-orbit coupling. So far, the monolayer/substrate coupling, which can manifest itself in strain, deformation, and hybridization, has proven to be detrimental to the aspired QSHE conditions for the monolayer. For stanene, the Sn analog of graphene, we investigate how an interposing buffer layer mediates between monolayer and substrate in order to optimize the QSHE setting. From a detailed density functional theory study, we highlight the principal mechanisms induced by such a buffer layer to accomplish quasifreestanding stanene in its QSHE phase. We complement our theoretical predictions by presenting attempts to grow a buffer layer on SiC(0001) on which stanene can be deposited.

DOI: 10.1103/PhysRevB.99.035145

I. INTRODUCTION

Quantum spin Hall (QSH) systems are two-dimensional bulk nonconducting materials featuring topologically nontrivial conducting edge modes, whose stability against external perturbations is ensured by time reversal symmetry [1,2]. After the first theoretical prediction in graphene by Kane and Mele [3,4] and the subsequent prediction and experimental realization in HgTe/CdTe quantum wells [5,6], it became evident that the small bulk energy gap represents the hardest obstacle to render QSH materials operative at room temperature and, as such, relevant to technological applications.

An initial plausible way of increasing the bulk gap is to enhance the spin-orbit coupling strength of the constituting atoms. Within the group-IV elements, freestanding honeycomblike structures made by Si, Ge, and Sn atoms, dubbed silicene, germanene, and stanene, respectively, were estimated in theory to exhibit gaps up to 100 meV [7–9]. A realistic implementation, however, always requires the stabilization of freestanding 2D layers on a supporting substrate, with no guarantee that the resulting symmetry breaking keeps the QSH phase intact. For instance, this detrimental effect to the QSHE phase is seen when an insulating MoS_2 substrate stabilizes the growth of germanene [10] or a Bi_2Te_3 template is used to accommodate stanene flakes [11]. In both cases, the topological bulk gap does not survive the interaction with the substrate and either yields a metallic or trivially insulating monolayer.

By contrast, a constructive effect of the substrate is observed for bismuthene on SiC [12]. There, the strong hybridization between the substrate and the Bi π orbitals leaves a sizable topological bulk gap of 0.8 eV, highlighting bismuthene as the first material realization of a QSH system operable at ambient temperature. Monolayer WTe_2 is another recent example where the interaction between the 2D layer and the substrate stabilizes the QSH phase by opening a finite gap, thus avoiding contributions from the bulk material which may be detrimental to the edge conductivity [13–15].

On the basis of these observations, it is evident that any meaningful theoretical investigation must properly take the role of substrates into consideration. With a particular focus on stanene, several studies have attempted to include these effects [11,16–19], while only a few of them have considered technologically achievable, and hence relevant, substrates [18,19]. Rather, our objective is to address commercial wafers of wide-gap semiconductors as possible substrate candidates, in order to follow the motif of reaching proposals that might allow for the integration of QSH physics into ambient life devices. SiC(0001) turns out to be a promising way along this direction [20]. However, dangling bond passivation is a well-known problem of semiconductor surfaces. The presence of highly reactive surface charge may be detrimental to the QSH phase. Recent theoretical investigations proceeded by removing the effect of the dangling bonds via hydrogen (H) saturation [18,21]. Despite its modeling efficiency, this cannot be considered a viable solution, since no evidence of a 2D material grown on a pure H-saturated surface has so far been reported in the literature.

For silicene and germanene, several studies report on attempts of reducing the interaction with the substrate [22–27]. Regarding carbon, one monolayer deposited on SiC does not form graphene, as the symmetries and electronic properties are destroyed by the strong binding. Moving towards almost freestanding graphene, one can either grow further carbon

*domenico.disante@physik.uni-wuerzburg.de

on this first layer, which in fact takes care of saturating the dangling bonds, or intercalate "spacers" such as H, Au, or O between the first layer and the substrate [28–34]. Here, we explore another possibility, namely realizing the QSH phase in stanene on SiC(0001) by the insertion of a buffer layer of group-III and group-V elements. This way, the valence electrons from the buffer atoms saturate the SiC dangling bonds, keeping at the same time a favorable lattice matching. The positive effect of the buffer is counterbalanced by an unavoidable monolayer/substrate hybridization which, as we will explicate in the following, turns out not to damage the QSHE under particular conditions, and instead to even structurally stabilize stanene.

For buckled geometries, as it is also the case for stanene, a concomitant staggered potential (Semenoff mass [35]) emerges, which for specific buffers is strong enough to prevent the QSH formation [3]. Via a proper choice of the buffer characteristics, we tune the quantitative impact of the Semenoff mass term. While our DFT calculations show that on Al, Ga, In, and Tl, stanene is topologically trivial, we successfully minimize the detrimental effect of the Semenoff mass through switching to buffers made of group-V elements. Our calculations indeed demonstrate that the topology in stanene can be comfortably stabilized for buffer layers made of P and As atoms, which might stimulate further experimental progress along this direction.

II. METHODS

For our theoretical study of stanene on buffered SiC(0001) we employ state-of-the-art first-principles calculations based on density functional theory as implemented in the Vienna *ab initio* simulation package (VASP) [36], within the projector-augmented-plane-wave (PAW) method [37,38]. The generalized gradient approximation as parametrized by the PBE-GGA functional for the exchange-correlation potential is used [39], as well as different flavors of revised and van der Waals corrected functionals [40–43], by expanding the Kohn-Sham wave functions into plane waves up to an energy cutoff of 300 eV. We sample the Brillouin zone on an $8 \times 8 \times 1$ regular mesh, and if applicable, spin-orbit coupling (SOC) is self-consistently included [44]. Even though the stanene low-energy models are extracted by projecting onto Sn p_z- and sp_2-type maximally localized Wannier functions (MLWF) by using the WANNIER90 package [45], we compute the $\mathbb{Z}_2$ topological invariant following the general method by Soluyanov and Vanderbilt [46] as in the Z2PACK code. That is, without relying on any precomputed low-energy model, we directly compute the Wilson loop of the entirely occupied *ab initio* spectrum [47]. Phonon dispersions are obtained within the context of the frozen phonon method [48] as implemented in the PHONOPY code [49] with a $2 \times 2 \times 1$ supercell (as explained in the next paragraph, the unit cell consists already of 3×3 SiC and 2×2 stanene superstructures).

Each atom from group III and V can saturate three dangling bonds from the SiC surface, either from Si atoms of the Si-terminated SiC or from C atoms from the C-terminated SiC, as shown in Fig. 1(b). This requires a minimal $\sqrt{3} \times \sqrt{3}R(30^\circ)$ reconstruction, whose Brillouin zone and crystal structure are reported in Fig. 1(a). Moreover, a 2×2

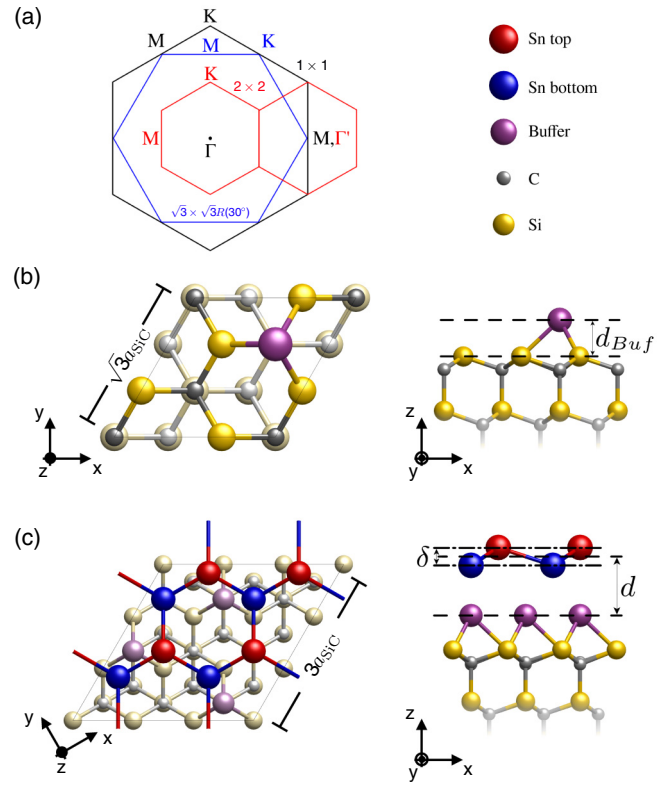

FIG. 1. (a) Brillouin zones of $\sqrt{3} \times \sqrt{3}R(30^\circ)$ SiC (blue), 1×1 stanene (black), and 2×2 stanene (red), with relative high symmetry points. (b) Top and side views of the crystalline structure of buffered $\sqrt{3} \times \sqrt{3}R(30^\circ)$ SiC and (c) 2×2 stanene/3×3 buffered SiC. The bottom termination of the slab models is artificially passivated by H atoms. In the top view in panel (c) the colors of the substrate are intentionally less intense compared to panel (b) in order to emphasize the hexagonal lattice of 2×2 stanene.

hexagonal lattice of stanene ($a = 9.28$ Å) turns out to have a good commensuration with a 3×3 reconstruction of SiC (lateral compressive strain $\varepsilon \sim 0.62\%$), suggesting a promising strain-free overlayer deposition. A 3×3 *buffered* SiC template ultimately shows at its surface a triangular lattice of buffer atoms [see Fig. 1(c)].

The large structural reconstructions enforce a folding of the electronic states into the supercell Brillouin zones, which map onto the primitive 1×1 Brillouin zones as sketched in Fig. 1(a). It is usually simpler to achieve a transparent physical description in the latter setting, where the unfolded band structure readily compares with the freestanding models when the symmetry breaking induced by the reconstruction is weak. The unfolding procedure we adopt in this work follows the lines described in Refs. [50,51].

For the experimental realization of a buffer layer we use n-doped (0.01–0.03 Ωcm) Si-terminated 4H-SiC(0001) wafer pieces. To prepare an atomically smooth, well-ordered substrate surface on large scales, the wafer pieces undergo a dry-etching process in a helium diluted hydrogen atmosphere with a flow of two standard liter per minute at 950 mbar and temperatures around 1200 °C for roughly 10 minutes. Subsequently, the H-terminated SiC(0001) samples [21] were transferred to the preparation chamber (base pressure

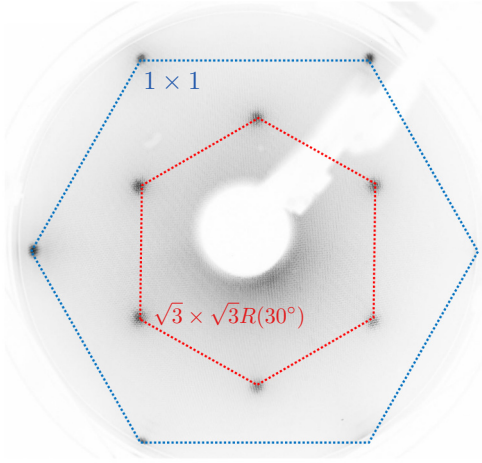

FIG. 2. LEED image of Al $\sqrt{3} \times \sqrt{3}R(30^\circ)$ on Si-terminated 4H-SiC(0001) recorded with an electron energy of 40 eV. Hexagons in red and blue highlight the Al induced $\sqrt{3} \times \sqrt{3}R(30^\circ)$ and 1×1 spots, respectively.

$p < 3 \times 10^{-11}$ mbar) using a vacuum suitcase. Surface quality was inspected *in situ* by low-energy electron diffraction (LEED).

Prior to the epitaxial growth of Al, the H termination of SiC(0001) has to be removed. This is achieved by heating the substrate to ∼620 °C with a subsequent cooling to ∼350 °C in the Al beam of the effusion cell, to form the Al $\sqrt{3} \times \sqrt{3}R(30^\circ)$ lattice, as shown in Fig. 2, where LEED clearly shows the reconstruction of the commensurate buffer layer. All samples were heated by direct current and the temperatures were measured pyrometrically.

III. STANENE ON GROUP-III BUFFER

A. Buffer analysis

We consider Al, Ga, In, and Tl as group III elements of the periodic table, which all share the same s^2p^1 valence electronic configuration. It has been shown that Al and other group III atoms can saturate the (111) surface of a silicon crystal, inducing a $\sqrt{3} \times \sqrt{3}R(30^\circ)$ reconstruction [52–55]. The underlying mechanism is that the three Al valence orbitals saturate three of the Si surface dangling bonds, which naturally leads to a $\sqrt{3} \times \sqrt{3}$ coverage of the Si substrate. By analogy, and based on the similarities that the SiC electronic structure shares with Si, we assume here that the deposition of group-III atoms induces on the SiC surface the same $\sqrt{3} \times \sqrt{3}R(30^\circ)$ reconstruction as on silicon. Our theoretical assumption is indeed experimentally proven here for the case of an Al buffer on SiC. Figure 2 shows a clear $\sqrt{3} \times \sqrt{3}R(30^\circ)$ reconstruction (red hexagon) on an underlying 1×1 template (blue hexagon).

The sp^3 orbitals of Al on SiC host the three valence electrons. The fourth one is empty and of sp_z-type character and gives rise to an antibonding in-gap state. The resulting band structures for this type of buffer layers on SiC (Si face) are shown in Fig. 3(a). The energy position of the antibonding in-gap state anticorrelates with the bonding distance of the buffer atom to SiC, as we show in Fig. 3(b). The lighter the buffer atom the shorter is the resulting distance, with the concomitant upward level repulsion of the antibonding orbital. This anticorrelation trend is independent of the SiC termination, holding both for the Si- and for the C-terminated surface.

In Fig. 3(a), in the case of the Al buffer on the Si face, in addition to the equilibrium Al-SiC distance $d_{\mathrm{Buf}} = 1.7$ Å, we show the bonding-antibonding in-gap states with predominant buffer character for two more values of d_{Buf}. If we lift Al to distances close to those obtained for Tl, the

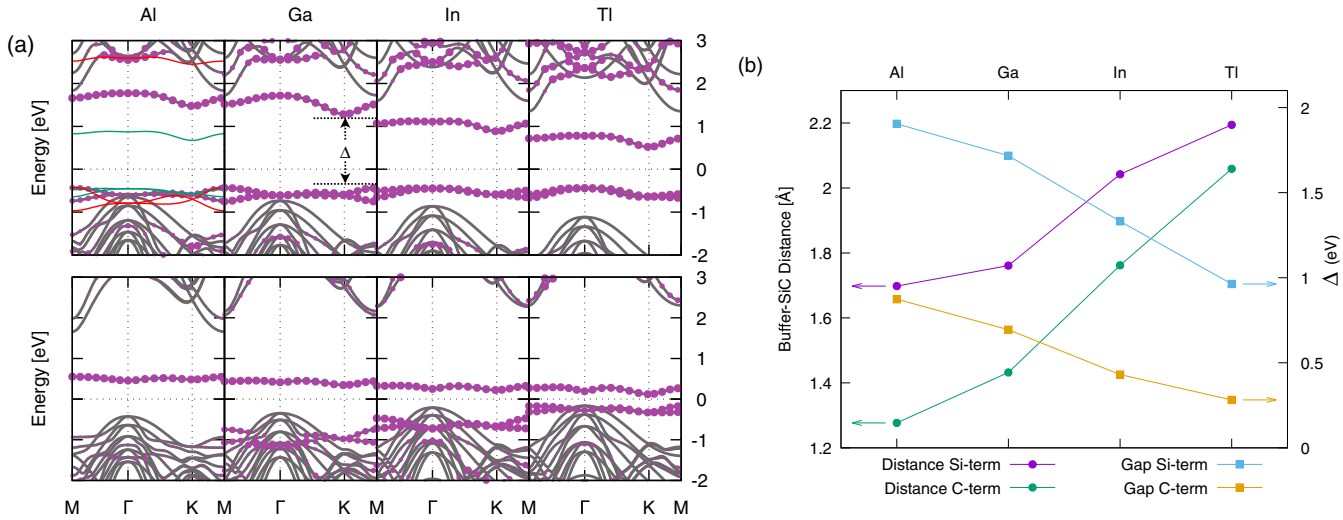

FIG. 3. (a) Electronic band structures for group III buffered SiC (top row for Si-face and bottom row for C-face SiC) along the high-symmetry lines of the $\sqrt{3} \times \sqrt{3}R(30^\circ)$ Brillouin zone [see Fig. 1(a)]. The colored dots highlight the orbital contribution from the buffer atom. For Al we additionally show the dependence of the bonding-antibonding in-gap states on the Al-SiC distance d_{Buf}: green corresponds to $d_{\mathrm{Buf}} = 2.1$ Å, i.e., roughly the same equilibrium distance obtained for Tl, while red corresponds to an exaggeratedly small value $d_{\mathrm{Buf}} = 1.3$ Å. (b) Anticorrelation of the bonding-antibonding states gap with the distance between the group-III atom buffer layer and the SiC surface, shown for both substrate terminations (Si and C faces).

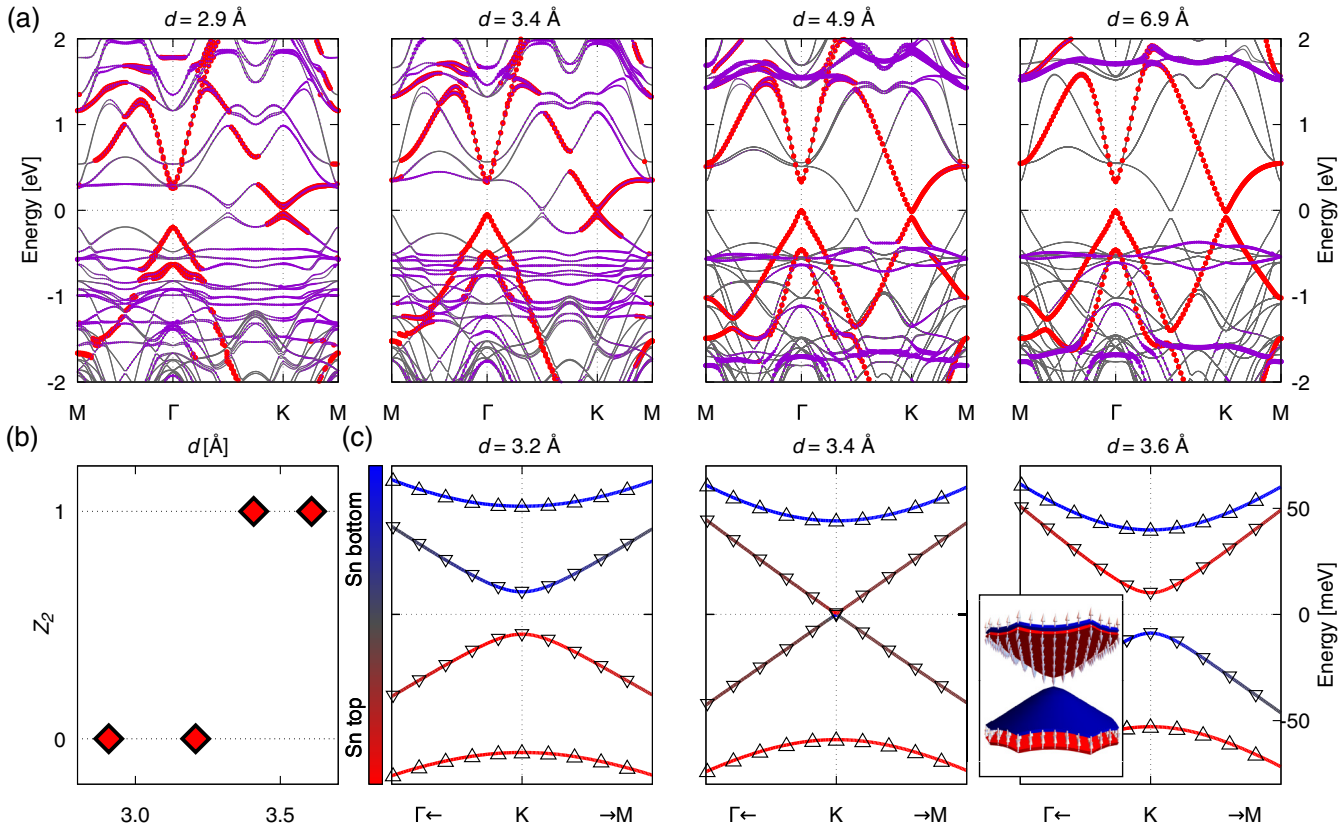

FIG. 4. (a) Evolution of the stanene/Al/SiC electronic band structure at different stanene-Al buffer distances (d = 2.9 Å, 3.4 Å, 4.9 Å, and 6.9 Å from left to right panels). Red dots highlight the unfolding weight from the 2 × 2 Brillouin zone onto the primitive 1 × 1, while the violet color code refers to the orbital contribution from the buffer atoms. (b) Behavior of the $\mathbb{Z}_2$ topological invariant close to the critical transition distance d_{cr}. (c) Zooms around the K point across the topological transition. Red and blue colors refer to orbital character from top and bottom Sn atoms, respectively. In the inset we report a three-dimensional view of the spin texture. The in-plane S_x and S_y components are negligible compared to the out-of-plane S_z component.

bonding-antibonding states are located at a very similar position with a comparable gap Δ (green curve). On the other hand, by pushing the buffer artificially close to SiC (d_{Buf} = 1.3 Å, red curve), Δ increases, with the antibonding state merging into the SiC conduction band. This evidences a rather weak dependence of the buffer states on the atomic species, proving that they instead decisively depend on d_{Buf}.

The energy position of the antibonding buffer level, and in turn the excitation gap, affect the strength of the hybridization when we add the stanene monolayer on top: The larger the gap of the SiC+buffer system is, the more strongly the buffer (conduction and valence) states hybridize with SiC. This implies that for a large Δ, the corresponding buffer states penetrate more pronouncedly into the bulk, and their surface localization is reduced. Stanene will hence be less affected in this situation. In the opposite case of a narrow gap, with buffer states situated at low energies, these have more weight at the surface and we expect sizable interaction effects between the buffer and stanene. A further important consequence is that top and bottom Sn atoms of the buckled inversion-breaking geometry have significantly distinct energy levels, as they are differently exposed to a strong interface potential. In Sec. IV we are going to show explicitly that this directly translates into the presence of a staggered potential term (Semenoff mass). This is known to be detrimental to the QSH phase, as it tends to compete with the second-nearest neighbor SOC [3].

B. Group-III buffered SiC + stanene

We now analyze the behavior of stanene, in particular its geometrical and its topological properties, when deposited on the group-III buffer layer. For the sake of clarity, we derive most of the following conclusion by focusing on the specific case of the Al buffer on SiC. The main purpose is to understand the physical mechanisms behind the interaction between stanene and the buffered substrate. With this in mind, we monitor the evolution of the electronic band structure of stanene as its bonding distance is artificially tuned from an unrealistically large value down to the equilibrium one $d_{\mathrm{eq}} \sim 2.9$ Å [see Fig. 4(a)]. The 2 × 2 structure reconstruction induced by the lattice commensuration leads to band foldings [50]. When the stanene-substrate distance is large enough to reduce the hybridization effects and the Coulomb interaction, we recover the freestanding stanene electronic properties. By unfolding the stanene band structure from the 2 × 2 Brillouin zone into the primitive 1 × 1, we can directly compare with the results of the freestanding description [8]. The reduction of the distance towards the equilibrium geometry and the

TABLE I. Summary of the DFT results obtained for buffer layers made of group III elements (for a geometry of stanene with preserved hexagonal symmetry). Si and C refer to the silicon and carbon terminated SiC, respectively. ΔE_K is the stanene energy gap at the K point. The dash symbol indicates that the system is metallic. d_{Buf}, d, and δ are the buffer layer-SiC distance, the stanene-buffer distance, and the buckling height, respectively. λ_v and $3\sqrt{3}\lambda_{SO}$ are the Semenoff mass and the effective SOC entering the Hamiltonian at the K point as given in Eq. (3), respectively. We also report the values of the $\mathbb{Z}_2$ invariant, even though in the case of group III this is always 0 at $d = d_{eq}$. The calculations are performed within GGA-PBE [39]. In the trivial $\mathbb{Z}_2 = 0$ phase, $\Delta E_K = 2[\lambda_v - 3\sqrt{3}\lambda_{SO}]$.

		Al	Ga	In	Tl
Si					
	ΔE_K (meV)	56	66	60	63
	d_{Buf} (Å)	1.7	1.8	2.0	2.2
	d (Å)	2.9	2.9	3.0	3.1
	δ (Å)	0.44	0.48	0.48	0.48
	$\mathbb{Z}_2$	0	0	0	0
	λ_v (meV)	49	58	50	52
	$3\sqrt{3}\lambda_{SO}$ (meV)	21	25	20	21
C					
	ΔE_K (meV)				
	d_{Buf} (Å)	1.3	1.4	1.8	2.1
	d (Å)	2.8	2.8	3.0	3.1
	δ (Å)	0.44	0.48	0.48	0.48
	$\mathbb{Z}_2$				

concomitant interaction causes the opening of hybridization gaps in the stanene band structure. Along with it, we find a distribution (spread) of stanene character over the Al/SiC electronic states. When the distance becomes smaller than the critical value $d_{cr} \sim 3.2$ Å, we observe a switching of the $\mathbb{Z}_2$ invariant from 1 to 0 [Fig. 4(b)]. This evidence marks the transition from freestandinglike topologically nontrivial to topologically trivial stanene, at least within GGA framework. As we will see in the following, the same mechanism leads to a different outcome in the case of group V.

A change in the topological invariant can only occur through an inversion of the bulk gap [1,2]. This evolution is indeed what we observe and show in Fig. 4(c). First of all, the breaking of the inversion symmetry induced by the presence of the substrate removes the band degeneracies at the K points. This effect goes under the name of valley-contrasting physics, or valleytronics, and is a well-known property of gated graphene and transition metal dichalcogenides [56,57]. The gap closure is accompanied by a change in the sublattice character of the bands. In fact, in the topological (trivial) phase, the contribution from the bottom Sn (top Sn) atom dominates the valence band maximum and vice versa for the conduction band minimum. The closure of the gap occurs through a linear Dirac-like band touching where the sublattice character is equally mixed, as highlighted by the brownish color of the linear branches in the middle panel of Fig. 4(c).

In the next section, we will establish an analogy with the topological transition as described by the Kane and Mele model [3] and analyze the quantitative role of the Semenoff mass. Note that the trend observed here for stanene on Al/SiC is common to all the group-III buffer setups, regardless of the SiC termination (see Table I). As shown in Fig. 3(b), it holds that the heavier the buffer atom deposited on SiC, the smaller the bulk gap. For this reason, the most favorable group-III buffer for growing quasifreestanding stanene is Al. The latter leads, however, to a topologically trivial configuration for stanene, demonstrating how going downwards in the "triels" group of the periodic table is not a promising approach to obtain $\mathbb{Z}_2 = 1$.

IV. ROLE OF THE SEMENOFF MASS

Interpreted within the framework of the Kane and Mele model [3], our tight-binding Hamiltonian reads

$$\begin{aligned} H = & t \sum_{\langle ij\rangle,\alpha} c^\dagger_{i,\alpha} c_{j,\alpha} + i\lambda_{SO} \sum_{\langle\langle ij\rangle\rangle,\alpha\alpha'} \nu_{ij} c^\dagger_{i,\alpha} s^z_{\alpha\alpha'} c_{j,\alpha'} \\ & + i\lambda_R \sum_{\langle ij\rangle,\alpha\alpha'} c^\dagger_{i,\alpha} (\mathbf{s}\times\hat{\mathbf{d}}_{ij})^z_{\alpha\alpha'} c_{j,\alpha'} \\ & + \lambda_v \sum_{i,\alpha} \xi_i c^\dagger_{i,\alpha} c_{i,\alpha}, \end{aligned} \tag{1}$$

where the first is a nearest neighbor hopping term on the honeycomb lattice and the second a mirror symmetric SOC one (here $\nu_{ij}\hat{\mathbf{u}}_z = (2/\sqrt{3})(\hat{\mathbf{d}}_1 \times \hat{\mathbf{d}}_2)$ where $\hat{\mathbf{d}}_{1,2}$ are unit vectors along the two bonds from site j to site i, and $\hat{\mathbf{u}}_z$ is a unit vector perpendicular to the stanene plane), and $\mathbf{s}$ are the Pauli matrices for the electron spin. The third term is a nearest-neighbor Rashba coupling due to a perpendicular electric field or to an interaction with a substrate and the last term sets the staggered potential (Semenoff mass) λ_v ($\xi_i = \pm 1$ depending on the sublattice). The latter differentiates the on-site energies of the two atoms constituting the bipartite honeycomb lattice. Without the Rashba term, the momentum-space Hamiltonian assumes the form

$$\begin{aligned} H(\mathbf{k}) = & t(1 + 2\cos x \cos y)\Gamma_1 - 2t \cos x \sin y \Gamma^{12} \\ & + \lambda_{SO}(2\sin 2x - 4 \sin x \cos y)\Gamma^{15} + \lambda_v \Gamma_2 \end{aligned} \tag{2}$$

with $x = k_x a/2$ and $y = \sqrt{3}k_y a/2$ (a being the hexagonal unit cell lattice constant, i.e., $\overline{\langle ij\rangle} = a/\sqrt{3}$), $\Gamma_1 = \sigma_x \otimes s_0$, $\Gamma_2 = \sigma_z \otimes s_0$, and $\Gamma_5 = \sigma_y \otimes s_z$ three of the five Dirac matrices with σ_i describing the sublattice degree of freedom and $\Gamma^{ab} = [\Gamma_a, \Gamma_b]/2i$. At the K point, the Hamiltonian is diagonal in the sublattice basis $A\uparrow, B\uparrow, A\downarrow, B\downarrow$:

$$\begin{bmatrix} \lambda_v - 3\sqrt{3}\lambda_{SO} & 0 & 0 & 0 \\ 0 & -(\lambda_v - 3\sqrt{3}\lambda_{SO}) & 0 & 0 \\ 0 & 0 & \lambda_v + 3\sqrt{3}\lambda_{SO} & 0 \\ 0 & 0 & 0 & -(\lambda_v + 3\sqrt{3}\lambda_{SO}) \end{bmatrix}. \tag{3}$$

The two ↑ and the two ↓ eigenvalues with smaller and larger splitting, respectively, give a perfect account of the four bands visible in the actual DFT calculation [Fig. 4(c)]. The matching between the DFT result and the Kane-Mele model can be pushed further upon comparing the sublattice character of these four eigenvalues and its evolution with d. We define $d_{\rm cr}$ as the distance at which the two lowest-lying DFT eigenvalues touch each other. For $d < d_{\rm cr}$ the character of both the uppermost eigenvalues is on one sublattice, namely the one corresponding to the bottom Sn atom, while both eigenvalues in the valence band belong to the top Sn. For $d > d_{\rm cr}$ the sublattice character at the K point is instead interchanged, a situation which in the mapping onto the Kane-Mele is obtained in the QSH phase for values of the Semenoff mass $\lambda_v < 3\sqrt{3}\lambda_{\rm SO}$ [3]. In the topological phase with inverted sublattice character, the lattice site with the highest on-site energy ($+\lambda_v$) contributes to the valence band maximum at K, at odds with the trivial atomic limit.

Let us note that the inversion of sublattice character is well defined only at the K and K′ points, where the Kane-Mele Hamiltonian is diagonal in the original basis. A suitable definition of the character over the whole Brillouin zone can be obtained by rotating the Kane-Mele Hamiltonian at each k point in the basis of the eigenvectors of (2) calculated at $\lambda_{\rm SO} = 0$. At the Γ point, for instance, the Kane-Mele model is made of two identical 2×2 blocks, with $\pm\lambda_v$ on the diagonal and $3t$ between the A and B sites. Going away from the Γ point and continuing to use the "bonding"-"antibonding" basis defined above, the SOC acquires off-diagonal elements which mix the "bonding"-"antibonding" eigenvectors approaching K and K′ leading to the inversion at the topological phase transition.

So far we have discussed the qualitative correspondence between the Kane-Mele model and the DFT results. Now, we make a more quantitative comparison by estimating the Semenoff mass and SOC term via a fit of the DFT eigenvalues at the K point with the analytic expressions given in Eq. (3). For the Al buffer, at $d_{\rm eq}$, we extract a difference between the p_z onsite energies of the top- and bottom-Sn atoms of $2\lambda_v = 0.098$ eV. The highest levels belong to the bottom Sn atoms that feel the buffer layer stronger than the top ones and are hence pushed up in energy. In the Kane-Mele Hamiltonian $\lambda_{\rm SO}$ represents a nonlocal term which accounts for the coupling of orbitals with parallel spin on the same sublattice. However, a finite buckling angle introduces a nonvanishing local contribution to the SOC [58]. We estimate that, in stanene on Al/SiC, $3\sqrt{3}\lambda_{\rm SO} \sim 21$ meV. Therefore, the relationship $\lambda_v > 3\sqrt{3}\lambda_{\rm SO}$ holds for stanene on the Al buffer at the equilibrium distance, confirming the trivial ground state found in our DFT computations. As can be inferred from Table I, the same relationship holds for all the investigated group-III buffers.

Let us briefly comment on the quantitative estimate of the Semenoff mass: An alternative way of extracting the staggered potential is from the difference of the p_z-local levels of the two sublattices via a Wannier projection of the DFT band structure. In order to get a satisfactory agreement with DFT, the projection must contain all the p orbitals of tin as well as orbitals from the buffer atoms. This means that the resulting Wannier Hamiltonian is defined on a much larger Hilbert space than the one of the Kane-Mele model, which assumes one single orbital per site. To directly connect to λ_v, one would have to further downfold the Wannier Hamiltonian onto a p_z-type low-energy model. A direct projection onto such a minimal model, however, turns out to yield a poor correspondence with the DFT bands. Furthermore, there is another argument in favor of an extended local basis, namely that this allows us to disentangle hybridization effects stemming from the buffer. As described above, we adopt the simpler procedure based on the fit of the DFT eigenvalues at the K point to the analytic results of Eq. (3).

In the previous analysis, we have neglected the Rashba coupling in Eq. (1). The presence of a finite λ_R mixes the ↑ and ↓ blocks of the Hamiltonian breaking the conservation of the z component of the spin. Moreover, a chiral spin texture appears around the K point. We checked that this effect is negligible, as shown in the inset to Fig. 4(c), proving that our assumption $\lambda_R = 0$ is justified and does not affect the qualitative arguments given above. Let us additionally note that, as recently demonstrated, the impact of the Rashba coupling in 2D superstructures can be reduced by a proper choice of the lattice commensuration [59].

V. STANENE ON GROUP-V BUFFER

Equipped with the microscopic understanding gained in the previous section of the mechanism responsible for the topological transition in stanene on the buffer layer, we shall now address the key question of our study: how to realize quasifreestanding topologically nontrivial stanene. From our analysis of group III, we have learned that the buffer in-gap states have to stay as far as possible away from E_F and, at the same time, the Semenoff mass term must be minimized. To limit the detrimental effect of these antibonding states, the corresponding bonds ought to be saturated. Two more valence electrons in the buffer exactly serve this purpose, offered by the p shell of group-V atoms.

In Fig. 5(a) we compare the density of the states (DOS) and band structure of Al/SiC and P/SiC (C face). From the comparison between the group-III and V buffer it is clear that our expectation of the quenching of the antibonding state is fulfilled: For group V we indeed observe a chemically inert lone pair characterized by a pronounced s-type orbital character [see inset in Fig. 5(a)]. This is located around 10 eV below the Fermi level, leaving as a consequence more "room" within the gap for an interference-free positioning of the stanene layer. Thanks to the reduced monolayer/substrate interaction, the induced Semenoff mass is indeed smaller. This is illustrated in Table II, where we summarize our results for stanene on group-V buffer/SiC substrates. All the calculated values of λ_v are sensibly reduced compared to the ones reported in Table I. Furthermore, contrary to group III, in the case of group V buffers the hexagonal symmetry of stanene is preserved during the relaxation, reflecting the much weaker hybridization strength.

Before moving to the analysis of the resulting electronic properties, we turn our attention to the nature of the bonding between stanene and the buffer layer. To this purpose, in Fig. 5(b) we show the binding energies of stanene on Al (left panel) and P (right panel) buffer/SiC within different levels of sophistication, explicitly including long-range dispersion to

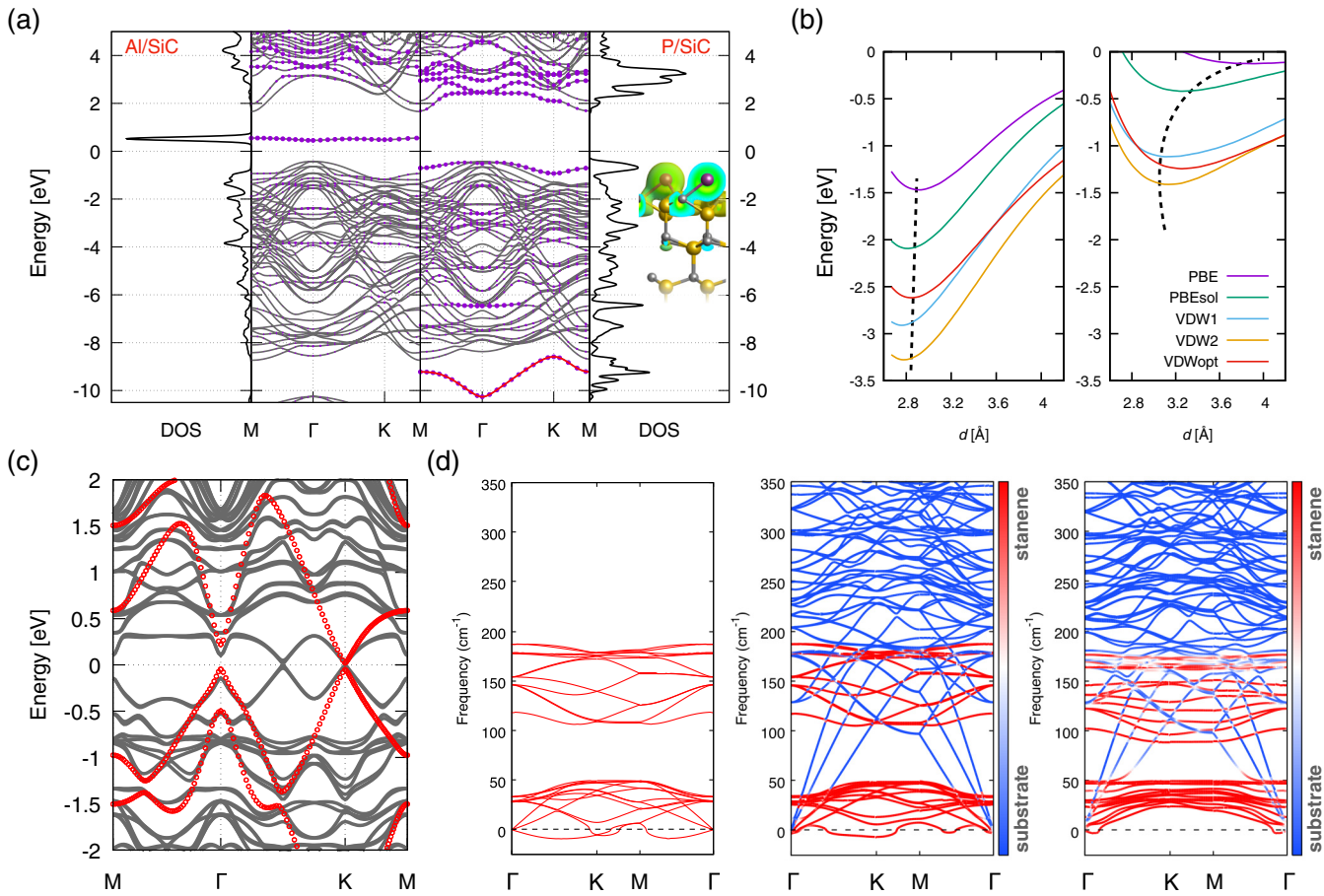

FIG. 5. (a) Buffer resolved density of the states and band structure of Al/SiC and P/SiC (C face hereafter in this caption), respectively. The dots in the band structure highlight the orbital weight of buffer atoms. In the inset, the charge distribution projected on the states forming the lone pair around 9 eV of binding energy for P/SiC is shown. (b) Binding energy curves for stanene on Al Si-terminated SiC (left panel) and on P C-terminated SiC (right panel) with and without different flavors of van der Waals corrected functionals (PBE [39], PBEsol [40], VDW1 [41], VDW2 [42], VDWopt [43]). The black dashed lines are guide to the eye to track the evolution of the equilibrium distance within the tested approximations. (c) band structure (with VDW1 van der Waals correction) of 2×2 stanene on P/SiC with the red dots referring to freestanding stanene in the primitive 1×1 structure. (d) Phonon spectra of freestanding stanene (leftmost panel) and stanene on P/SiC at the 3.9 Å PBE (central panel) and 2.9 Å VDW1 (rightmost panel) equilibrium distances. The color code refers to pure P/SiC (blue) and pure stanene (red) contributions to the phonon modes.

account for van der Waals interactions. The difference in the two behaviors suggests a distinct nature of the bonding. While on group III buffer/SiC van der Waals corrections do not change qualitatively the equilibrium geometry of stanene, a sizable reduction of the equilibrium distance occurs for group V buffer/SiC. Such an evidence hints at a strong covalent nature of the bonding on the group-III buffer, as a result of the hybridization between stanene and the antibonding in-gap state. On the other hand, the inert lone pair prevents from any form of chemical bonding, leaving room for the predominance of the van der Waals interaction.

The band structure of stanene on C-terminated P/SiC at the van der Waals equilibrium geometry is shown in Fig. 5(c). The Dirac physics around the K point resembles to a large extent the one of freestanding stanene [8]. Our conclusion is further substantiated by the explicit computation of the $\mathbb{Z}_2$ invariant (not shown), where a Kramers' pair switching indicates the nontrivial topological nature ($\mathbb{Z}_2 = 1$) [46].

Our calculations reveal that P and As buffer atoms on C-terminated SiC are ideal templates to host stanene in the QSH phase. The high electronegativity of carbon plays an important role. The resulting strengthening of the bonding of the buffer atoms to the substrate, and in turn of the hybridization between the in-gap bands and the continuum of SiC electronic states, sets favorable conditions for a topological ground state. We predict stanene to be a QSH on Bi as well, but it is likely that Bi on SiC prefers the 2/3 coverage, as recently reported in the case of bismuthene/SiC [12]. Stanene on Sb/SiC is right at the verge of the topological transition, being the gap at the K point not larger than ∼1 meV. The configurations on the other termination of SiC are instead metallic and in the cases of P and As, also highly distorted. Being less electronegative than C, Si attracts less negative charge from the buffer atoms compared to what C does, resulting in turn in a larger SiC/buffer distance d_{Buf} (see Table II). This confirms that the C face, in combination with group-V buffer layers,

TABLE II. Same as Table I but for buffer layers made of group-V elements. The column on the left refers to Si face or C face of the SiC substrate. The asterisk (*) in the entries of δ indicates that the stanene low-buckled hexagonal geometry is not preserved anymore and it is not possible to define a buckling parameter. The calculations are performed within the VDW1 framework [41]. In the topological $\mathbb{Z}_2 = 1$ phase, $\Delta E_K = 2[3\sqrt{3}\lambda_{SO} - \lambda_v]$.

		P	As	Sb	Bi
Si					
	ΔE_K (meV)				
	d_{Buf} (Å)	1.8	2.0	2.1	2.2
	d (Å)	1.9	1.7	3.0	3.2
	δ (Å)	*	*	0.40	0.43
	$\mathbb{Z}_2$				
C					
	ΔE_K (meV)	13	34	1	13
	d_{Buf} (Å)	1.2	1.4	1.6	1.8
	d (Å)	2.9	3.0	3.2	3.2
	δ (Å)	0.43	0.42	0.42	0.42
	$\mathbb{Z}_2$	1	1	1	1
	λ_v (meV)	16	6	19	10
	$3\sqrt{3}\lambda_{SO}$ (meV)	23	23	19	17

offers the ideal degree of hybridization to host stanene without spoiling the QSH phase.

Having assessed the possibility to achieve a topological ground state for stanene, an important issue is yet to be addressed. It is known that freestanding stanene as predicted in Ref. [8] is not dynamically stable in the low-buckled (LB) geometry of interest here [60]. This instability is a consequence of negative phonon frequencies that the flexural ZA mode has along the Γ-K and Γ-M directions, as shown in the leftmost panel of Fig. 5(d). The origin of negative frequencies is ascribed to the weak π-π bonding of LB stanene that fails to stabilize a buckled configuration. It is interesting to note how a dumbbell (DB) stanene configuration has been theoretically proposed to be stable and topologically nontrivial on a variety of different substrates [60]. At odds with LB stanene, however, in DB stanene the band inversion induced by the SOC occurs at the Γ point, and the Dirac-like physics at the K point is irredeemably spoiled.

The substrate engineering based on our buffer strategy turns out to be decisive to stabilize stanene in the LB configuration. As shown in the central and rightmost panels of Fig. 5(d), the interaction with the substrate reduces the negative phonon frequencies, eventually ending up in a stable configuration at the van der Waals equilibrium distance. In such a configuration, all the frequencies of phonon modes associated to stanene are positive. The small still imaginary frequencies in the long-wavelength $\mathbf{q} \to 0$ flexural acoustic ZA mode is a well known artifact that is not related to a structural instability [61–63]. The stabilization of the ZA phonon mode via interaction with the buffer is a result of the very nature of this mode, which in atomically thin systems involves a vertical bending of the layer, i.e., a flexural mode in the direction of the substrate. We cannot exclude at this point a high-buckled (HB) configuration of stanene, since it has been reported that for freestanding tin and lead monolayers, a metallic HB phase is energetically favorable against the LB one [64]. However, we stress again here that the role of the substrate, within the concept we propose in this work, is pivotal to accomplish a quasifreestanding LB phase, which is dynamically stable but still retains a QSH physics at the K point.

VI. CONCLUSIONS

Through a systematic first-principles analysis we have unveiled the mechanisms underlying the delicate QSH formation in stanene grown on a SiC(0001) substrate and how these growth conditions can be fundamentally improved by an appropriate buffer between substrate and monolayer. We followed the guiding principle that a technologically relevant substrate is crucial for any future integration of QSH systems in novel spin-based devices. SiC distinguishes itself as one of the most promising substrate candidates; we have accomplished a substrate engineering mechanism that employs a buffer layer for the saturation of the substrate dangling bonds. We have further revealed the microscopic processes that are deleterious to the formation of the topological phase, owing to the electronic hybridization between the substrate and the stanene monolayer. Combining these insights, we predict a stable QSH phase of stanene in the four cases of group-V buffered SiC.

By analyzing the hybridization between the stanene layer and the buffer, and by mapping the full *ab initio* Hamiltonian onto a generalized effective Hamiltonian including a staggered potential (Semenoff mass term), we show that some buffer layers are more suitable than others to protect the QSH formation in the monolayer. The strategy we follow then is to minimize the detrimental staggered potential by choosing such atoms which have their bonding and antibonding states energetically far away from the chemical potential. This leads us to concrete suggestions for promising buffer materials, in particular the use of group-V elements (P and As).

Note that our theoretical study only establishes a lower bound to the potential range of parameter space in which the QSH phase in stanene might be stabilized by proper substrate engineering. This is because our DFT approach utilizes the GGA approximation, which, due to the prohibitive size of the reconstructions we considered, would be extremely time consuming to replace it by alternative procedures. The use of GGA suggests that a ∼20% underestimation of the antibonding states energy position is possible [see Fig. 3(a)] and that some of the trivial configurations we have found (Tables I and II) are in fact still in the QSH domain. In terms of an explicit analysis of the buffer-assisted growth of stanene on SiC, we reported a detailed LEED pattern (Fig. 2) demonstrating a $\sqrt{3} \times \sqrt{3}R(30^\circ)$ reconstruction of SiC after Al deposition. Together, our efforts constitute promising steps towards the accomplishment for the realization of quantum spin Hall candidate materials through buffer engineering.

ACKNOWLEDGMENTS

The authors acknowledge G. Profeta for fruitful and inspiring discussions. This work was supported by the Deutsche Forschungsgemeinschaft (DFG) through

SFB1170 "ToCoTronics" and by ERC-StG-336012-Thomale-TOPOLECTRICS. We gratefully acknowledge the Gauss Centre for Supercomputing e.V. (www.gauss-centre.eu) for funding this project by providing computing time on the GCS Supercomputer SuperMUC at Leibniz Supercomputing Centre (www.lrz.de).

[1] M. Z. Hasan and C. L. Kane, Colloquium: Topological insulators, Rev. Mod. Phys. **82**, 3045 (2010).
[2] X.-L. Qi and S.-C. Zhang, Topological insulators and superconductors, Rev. Mod. Phys. **83**, 1057 (2011).
[3] C. L. Kane and E. J. Mele, Z_2 Topological Order and the Quantum Spin Hall Effect, Phys. Rev. Lett. **95**, 146802 (2005).
[4] C. L. Kane and E. J. Mele, Quantum Spin Hall Effect in Graphene, Phys. Rev. Lett. **95**, 226801 (2005).
[5] B. A. Bernevig, T. L. Hughes, and S.-C. Zhang, Quantum spin hall effect and topological phase transition in HgTe quantum wells, Science **314**, 1757 (2006).
[6] M. König, S. Wiedmann, C. Brüne, A. Roth, H. Buhmann, L. W. Molenkamp, X.-L. Qi, and S.-C. Zhang, Quantum spin hall insulator state in HgTe quantum wells, Science **318**, 766 (2007).
[7] A. Molle, J. Goldberger, M. Houssa, Y. Xu, S.-C. Zhang, and D. Akinwande, Buckled two-dimensional Xene sheets, Nat. Mater. **16**, 163 (2017).
[8] Y. Xu, B. Yan, H.-J. Zhang, J. Wang, G. Xu, P. Tang, W. Duan, and S.-C. Zhang, Large-Gap Quantum Spin Hall Insulators in Tin Films, Phys. Rev. Lett. **111**, 136804 (2013).
[9] F. Geissler, J. C. Budich, and B. Trauzettel, Group theoretical and topological analysis of the quantum spin hall effect in silicene, New J. Phys. **15**, 085030 (2013).
[10] L. Zhang, P. Bampoulis, A. N. Rudenko, Q. Yao, A. van Houselt, B. Poelsema, M. I. Katsnelson, and H. J. W. Zandvliet, Structural and Electronic Properties of Germanene on MoS_2, Phys. Rev. Lett. **116**, 256804 (2016).
[11] F.-F. Zhu, W.-J. Chen, Y. Xu, C.-L. Gao, D.-D. Guan, C.-H. Liu, D. Qian, S.-C. Zhang, and J.-F. Jia, Epitaxial growth of two-dimensional stanene, Nat. Mater. **14**, 1020 (2015).
[12] F. Reis, G. Li, L. Dudy, M. Bauernfeind, S. Glass, W. Hanke, R. Thomale, J. Schäfer, and R. Claessen, Bismuthene on a SiC substrate: A candidate for a high-temperature quantum spin Hall material, Science **357**, 287 (2017).
[13] X. Qian, J. Liu, L. Fu, and J. Li, Quantum spin Hall effect in two-dimensional transition metal dichalcogenides, Science **346**, 1344 (2014).
[14] S. Tang, C. Zhang, D. Wong, Z. Pedramrazi, H.-Z. Tsai, C. Jia, B. Moritz, M. Claassen, H. Ryu, S. Kahn, J. Jiang, H. Yan, M. Hashimoto, D. Lu, R. G. Moore, C.-C. Hwang, C. Hwang, Z. Hussain, Y. Chen, M. M. Ugeda, Z. Liu, X. Xie, T. P. Devereaux, M. F. Crommie, S.-K. Mo, and Z.-X. Shen, Quantum spin Hall state in monolayer WTe_2, Nat. Phys. **13**, 683 (2017).
[15] S. Ok, L. Muechler, D. Di Sante, G. Sangiovanni, R. Thomale, and T. Neupert, Custodial glide symmetry of quantum spin Hall edge modes in WTe_2 monolayer, arXiv:1811.00551.
[16] C.-Z. Xu, Y.-H. Chan, P. Chen, X. Wang, D. Flötotto, J. A. Hlevyack, G. Bian, S.-K. Mo, M.-Y. Chou, and T.-C. Chiang, Gapped electronic structure of epitaxial stanene on InSb(111), Phys. Rev. B **97**, 035122 (2018).
[17] Z. Ni, E. Minamitani, Y. Ando, and S. Watanabe, Germanene and stanene on two-dimensional substrates: Dirac cone and Z_2 invariant, Phys. Rev. B **96**, 075427 (2017).
[18] F. Matusalem, F. Bechstedt, M. Marques, and L. K. Teles, Quantum spin Hall phase in stanene-derived overlayers on passivated SiC substrates, Phys. Rev. B **94**, 241403 (2016).
[19] F. Matusalem, D. S. Koda, F. Bechstedt, M. Marques, and L. K. Teles, Deposition of topological silicene, germanene and stanene on graphene-covered SiC substrates, Sci. Rep. **7**, 15700 (2017).
[20] S. Glass, G. Li, F. Adler, J. Aulbach, A. Fleszar, R. Thomale, W. Hanke, R. Claessen, and J. Schäfer, Triangular Spin-Orbit-Coupled Lattice with Strong Coulomb Correlations: Sn Atoms on a SiC(0001) Substrate, Phys. Rev. Lett. **114**, 247602 (2015).
[21] S. Glass, F. Reis, M. Bauernfeind, J. Aulbach, M. R. Scholz, F. Adler, L. Dudy, G. Li, R. Claessen, and J. Schäfer, Atomic-Scale Mapping of Layer-by-Layer Hydrogen Etching and Passivation of SiC(0001) Substrates, J. Phys. Chem. C **120**, 10361 (2016).
[22] M. Houssa, G. Pourtois, V. V. Afanasév, and A. Stesmans, Can silicon behave like graphene? A first-principles study, Appl. Phys. Lett. **97**, 112106 (2010).
[23] M. Kanno, R. Arafune, C. L. Lin, E. Minamitani, M. Kawai, and N. Takagi, Electronic decoupling by h-BN layer between silicene and Cu(111): A dft-based analysis, New J. Phys. **16**, 105019 (2014).
[24] F. d'Acapito, S. Torrengo, E. Xenogiannopoulou, P. Tsipas, J. M. Velasco, D. Tsoutsou, and A. Dimoulas, Evidence for Germanene growth on epitaxial hexagonal (h)-AlN on Ag(111), J. Phys.: Condens. Matter **28**, 045002 (2016).
[25] Z. Ni, Q. Liu, K. Tang, J. Zheng, J. Zhou, R. Qin, Z. Gao, D. Yu, and J. Lu, Tunable bandgap in silicene and germanene, Nano Lett. **12**, 113 (2012).
[26] Y. Du, J. Zhuang, J. Wang, Z. Li, H. Liu, J. Zhao, X. Xu, H. Feng, L. Chen, K. Wu, X. Wang, and S. X. Dou, Quasi-freestanding epitaxial silicene on Ag(111) by oxygen intercalation, Sci. Adv. **2**, e1600067 (2016).
[27] T. P. Kaloni and U. Schwingenschlögl, Weak interaction between germanene and GaAs(0001) by H intercalation: A route to exfoliation, J. Appl. Phys. **114**, 184307 (2013).
[28] C. Virojanadara, S. Watcharinyanon, A. A. Zakharov, and L. I. Johansson, Epitaxial graphene on 6H-SiC and Li intercalation, Phys. Rev. B **82**, 205402 (2010).
[29] C. Enderlein, Y. S. Kim, A. Bostwick, E. Rotenberg, and K. Horn, The formation of an energy gap in graphene on ruthenium by controlling the interface, New J. Phys. **12**, 033014 (2010).
[30] S. Oida, F. R. McFeely, J. B. Hannon, R. M. Tromp, M. Copel, Z. Chen, Y. Sun, D. B. Farmer, and J. Yurkas, Decoupling graphene from SiC(0001) via oxidation, Phys. Rev. B **82**, 041411 (2010).
[31] F. Varchon, R. Feng, J. Hass, X. Li, B. N. Nguyen, C. Naud, P. Mallet, J.-Y. Veuillen, C. Berger, E. H. Conrad, and L. Magaud, Electronic Structure of Epitaxial Graphene Layers on SiC: Effect of the Substrate, Phys. Rev. Lett. **99**, 126805 (2007).

[32] S. Watcharinyanon, C. Virojanadara, J. Osiecki, A. Zakharov, R. Yakimova, R. Uhrberg, and L. Johansson, Hydrogen intercalation of graphene grown on 6H-SiC(0001), Surf. Sci. **605**, 1662 (2011).

[33] K. V. Emtsev, A. Bostwick, K. Horn, J. Jobst, G. L. Kellogg, L. Ley, J. L. McChesney, T. Ohta, S. A. Reshanov, J. Röhrl, E. Rotenberg, A. K. Schmid, D. Waldmann, H. B. Weber, and T. Seyller, Towards wafer-size graphene layers by atmospheric pressure graphitization of silicon carbide, Nat. Mater. **8**, 203 (2009).

[34] S. Y. Zhou, G.-H. Gweon, A. V. Fedorov, P. N. First, W. A. de Heer, D.-H. Lee, F. Guinea, A. H. Castro Neto, and A. Lanzara, Substrate-induced bandgap opening in epitaxial graphene, Nat. Mater. **6**, 770 (2007).

[35] G. W. Semenoff, Condensed-Matter Simulation of a Three-Dimensional Anomaly, Phys. Rev. Lett. **53**, 2449 (1984).

[36] G. Kresse and J. Furthmüller, Efficient iterative schemes for *ab initio* total-energy calculations using a plane-wave basis set, Phys. Rev. B **54**, 11169 (1996).

[37] G. Kresse and D. Joubert, From ultrasoft pseudopotentials to the projector augmented-wave method, Phys. Rev. B **59**, 1758 (1999).

[38] P. E. Blöchl, Projector augmented-wave method, Phys. Rev. B **50**, 17953 (1994).

[39] J. P. Perdew, K. Burke, and M. Ernzerhof, Generalized Gradient Approximation Made Simple, Phys. Rev. Lett. **77**, 3865 (1996).

[40] J. P. Perdew, A. Ruzsinszky, G. I. Csonka, O. A. Vydrov, G. E. Scuseria, L. A. Constantin, X. Zhou, and K. Burke, Restoring the Density-Gradient Expansion for Exchange in Solids and Surfaces, Phys. Rev. Lett. **100**, 136406 (2008).

[41] S. Grimme, Semiempirical gga-type density functional constructed with a long-range dispersion correction, J. Comp. Chem. **27**, 1787 (2006).

[42] A. Tkatchenko and M. Scheffler, Accurate Molecular van der Waals Interactions from Ground-State Electron Density and Free-Atom Reference Data, Phys. Rev. Lett. **102**, 073005 (2009).

[43] J. Klimeš, D. R. Bowler, and A. Michaelides, Chemical accuracy for the van der waals density functional, J. Phys.: Cond. Matt. **22**, 022201 (2010).

[44] S. Steiner, S. Khmelevskyi, M. Marsmann, and G. Kresse, Calculation of the magnetic anisotropy with projected-augmented-wave methodology and the case study of disordered $Fe_{1-x}Co_x$ alloys, Phys. Rev. B **93**, 224425 (2016).

[45] A. A. Mostofi, J. R. Yates, Y.-S. Lee, I. Souza, D. Vanderbilt, and N. Marzari, Wannier90: A tool for obtaining maximally-localised wannier functions, Comput. Phys. Commun. **178**, 685 (2008).

[46] A. A. Soluyanov and D. Vanderbilt, Computing topological invariants without inversion symmetry, Phys. Rev. B **83**, 235401 (2011).

[47] D. Gresch, G. Autès, O. V. Yazyev, M. Troyer, D. Vanderbilt, B. A. Bernevig, and A. A. Soluyanov, Z2pack: Numerical implementation of hybrid wannier centers for identifying topological materials, Phys. Rev. B **95**, 075146 (2017).

[48] K. Parlinski, Z. Q. Li, and Y. Kawazoe, First-Principles Determination of the Soft Mode in Cubic ZrO_2, Phys. Rev. Lett. **78**, 4063 (1997).

[49] A. Togo, F. Oba, and I. Tanaka, First-principles calculations of the ferroelastic transition between rutile-type and $CaCl_2$-type SiO_2 at high pressures, Phys. Rev. B **78**, 134106 (2008).

[50] W. Ku, T. Berlijn, and C.-C. Lee, Unfolding First-Principles Band Structures, Phys. Rev. Lett. **104**, 216401 (2010).

[51] M. Tomić, H. O. Jeschke, and R. Valentí, Unfolding of electronic structure through induced representations of space groups: Application to Fe-based superconductors, Phys. Rev. B **90**, 195121 (2014).

[52] J. Lander and J. Morrison, Surface reactions of silicon with aluminum and with indium, Surf. Sci. **2**, 553 (1964).

[53] J. E. Northrup, Si(111)$\sqrt{3} \times \sqrt{3}$-Al: An Adatom-Induced Reconstruction, Phys. Rev. Lett. **53**, 683 (1984).

[54] J. M. Nicholls, B. Reihl, and J. E. Northrup, Unoccupied surface states revealing the Si(111)$\sqrt{3}$ $\sqrt{3}$ -Al, -Ga, and -In adatom geometries, Phys. Rev. B **35**, 4137 (1987).

[55] R. J. Hamers, Effects of coverage on the geometry and electronic structure of Al overlayers on Si(111), Phys. Rev. B **40**, 1657 (1989).

[56] D. Xiao, W. Yao, and Q. Niu, Valley-Contrasting Physics in Graphene: Magnetic Moment and Topological Transport, Phys. Rev. Lett. **99**, 236809 (2007).

[57] D. Xiao, G.-B. Liu, W. Feng, X. Xu, and W. Yao, Coupled Spin and Valley Physics in Monolayers of MoS_2 and Other Group-VI Dichalcogenides, Phys. Rev. Lett. **108**, 196802 (2012).

[58] C.-C. Liu, H. Jiang, and Y. Yao, Low-energy effective Hamiltonian involving spin-orbit coupling in silicene and two-dimensional germanium and tin, Phys. Rev. B **84**, 195430 (2011).

[59] K. Song, D. Soriano, A. W. Cummings, R. Robles, P. Ordejón, and S. Roche, Spin proximity effects in graphene/topological insulator heterostructures, Nano Lett. **18**, 2033 (2018).

[60] P. Tang, P. Chen, W. Cao, H. Huang, S. Cahangirov, L. Xian, Y. Xu, S.-C. Zhang, W. Duan, and A. Rubio, Stable two-dimensional dumbbell stanene: A quantum spin hall insulator, Phys. Rev. B **90**, 121408 (2014).

[61] D. Liu, A. G. Every, and D. Tománek, Continuum approach for long-wavelength acoustic phonons in quasi-two-dimensional structures, Phys. Rev. B **94**, 165432 (2016).

[62] B. Peng, H. Zhang, H. Shao, Y. Xu, R. Zhang, and H. Zhu, The electronic, optical, and thermodynamic properties of borophene from first-principles calculations, J. Mater. Chem. C **4**, 3592 (2016).

[63] W. Yu, C.-Y. Niu, Z. Zhu, X. Wang, and W.-B. Zhang, Atomically thin binary v-v compound semiconductor: A first-principles study, J. Mater. Chem. C **4**, 6581 (2016).

[64] P. Rivero, J.-A. Yan, V. M. García-Suárez, J. Ferrer, and S. Barraza-Lopez, Stability and properties of high-buckled two-dimensional tin and lead, Phys. Rev. B **90**, 241408 (2014).